

Assessment of airborne transmission potential of COVID-19 by asymptomatic individuals under different practical settings

Authors: Siyao Shao^{1,2}, Dezhi Zhou¹, Ruichen He^{1,2}, Jiaqi Li^{1,2}, Shufan Zou¹, Kevin Mallery^{1,2}, Santosh Kumar^{1,2}, Suo Yang^{1, **}, Jiarong Hong^{1,2, *}

Affiliations:

¹Department of Mechanical Engineering, 111 Church ST SE, University of Minnesota, Minneapolis, MN, USA 55414.

²Saint Anthony Falls Laboratory, 2 3rd AVE SE, University of Minnesota, Minneapolis, MN, USA 55414.

*Email addresses of the first corresponding author: jhong@umn.edu

**Email addresses of the second corresponding author: suo-yang@umn.edu

The lack of quantitative risk assessment of airborne transmission of COVID-19 under practical settings leads to large uncertainties and inconsistencies in our preventive measures. Combining *in situ* measurements and numerical simulations, we quantify the exhaled aerosols from normal respiratory behaviors and their transport under elevator, small classroom, and supermarket settings to evaluate the risk of inhaling potentially virus-containing aerosols. Our results show that the design of ventilation is critical for reducing the risk of aerosol encounters. Inappropriate design can significantly limit the efficiency of aerosol removal, create local hot spots with orders of magnitude higher risks, and enhance aerosol deposition causing surface contamination. Additionally, our measurements reveal the presence of a substantial fraction of crystalline aerosols from normal breathing and its strong correlation with breathing depth.

One Sentence Summary: Ventilation plays a critical role in the risk of COVID-19 transmission via exhaled aerosols from asymptomatic individuals.

Main Text: The global pandemic of COVID-19 (caused by the SARS-CoV-2 virus) has demonstrated the extraordinary transmissibility of the virus, with more than 11 million people infected as of writing. However, mechanisms to contain the disease are regionally variable, with vastly different approaches being utilized by different countries, regions (such as US states), and even cities (1). This inconsistency is due in part to a lack of understanding of the transmission pathways of the disease (1). Although it has been well-accepted that the disease can be transmitted through large droplets ($>5\ \mu\text{m}$) capable of carrying sufficient viral load produced by coughing and sneezing (2, 3), there is substantial debate regarding whether the transmission can be airborne with small droplets (4-6). Nevertheless, growing evidence, including the detection of SARS-CoV-2 RNA in collected aerosols (7) and the ability of SARS-CoV-2 to remain viable for hours in aerosols (8), indicates such a transmission pathway is possible. Moreover, considering the high viral loads found in the upper respiratory tract of asymptomatic individuals infected with COVID-19 (9), it has been hypothesized that small droplets and particles (hereafter referred to collectively as aerosols) generated during normal respiratory behaviors, such as breathing and speaking, could lead to the fast spread of the disease (10-12). However, despite a number of studies of aerosol generation from these behaviors (12-17), there is a lack of *in situ* characterization, particularly for breathing due to its low yield of aerosol production, limiting our ability to model the spread of aerosols associated with asymptomatic individuals. Specifically, most research on the size distribution of such particles uses devices such as aerodynamic particle sizers (APS) and optical

particle counters (OPC) which require transporting the particles to the sensor and do not account for particle evaporation and particle losses during the transport (18). The only *in situ* measurement (14) utilize interferometric Mie imaging (IMI), which captures particles above 2 μm with measurement accuracy depending on the assumptions of particle refractive index and shape (assumed to be spherical). Accordingly, no study has conducted simulation of the change of size and concentration of aerosols over time and their spatial variation in an enclosed environment to provide quantitative assessment of the risk of airborne infection. These models are necessary for producing scientifically driven policy regarding social distancing measures and safe business re-opening.

Therefore, in the current study, we present the first detailed characterization of the aerosol generation process of normal human breathing by combining quantitative Schlieren imaging and multi-magnification digital inline holography (DIH). Such measurements, conducted with eight participants, provide the instantaneous and ensemble average flow field of exhaled gas as well as the concentration, size, and shape distributions of aerosols ranging from 0.5-50 μm within it. This information is then used as the inputs for high-fidelity numerical simulation of aerosol transport under several practical settings, which considers the evaporation, drag, gravity, and residence lifetime of each aerosol produced by a simulated asymptomatic individual. The simulation results are then used to assess the potential of airborne disease transmission associated with the normal respiratory behaviors under these settings.

The ensemble average flow field of exhaled gas (Fig. 1A), characterized using quantitative Schlieren imaging, shows an axisymmetric cone shape with an averaged cone angle ($\bar{\theta}$) of 25.0°. The streamwise flow velocity averaged over the cross section of the exhalation cone ($\overline{\langle u \rangle}$) decays from 0.3 m/s near the mouth to almost zero at about 200 mm (< 1 foot) downstream. These measurements demonstrate the limited spatial range of direct influence associated with normal breathing, in contrast to violent expiratory behaviors such as coughing which yield a cone angle of 65° (19) and flow speed up to 11.2 m/s with the influence zone extending up to ~2.5 m (20). The exhaled gas flow fields from different participants show similar patterns with small variation in quantitative measures (e.g. cone angle, exhaled flow rate, etc., Table S1 with details in the supplementary materials). Based on flow field measurements, the normalized exhaled gas flow rate (\hat{Q}_E) in an exhalation cycle (period T_E), rises sharply at the beginning of the cycle, peaks around 0.2 T_E followed by a sustained rate over a duration of about 0.3 T_E , and then decays rapidly (Fig. 1B). Such breathing pattern is similar across different participants as they are instructed to breath in the same fashion, but the peak value of \hat{Q}_E ($\hat{Q}_{E,\text{max}}$) varies substantially among individuals (Fig. S4 in the supplementary materials) potentially due to different natural breathing depths of each individual (21-23).

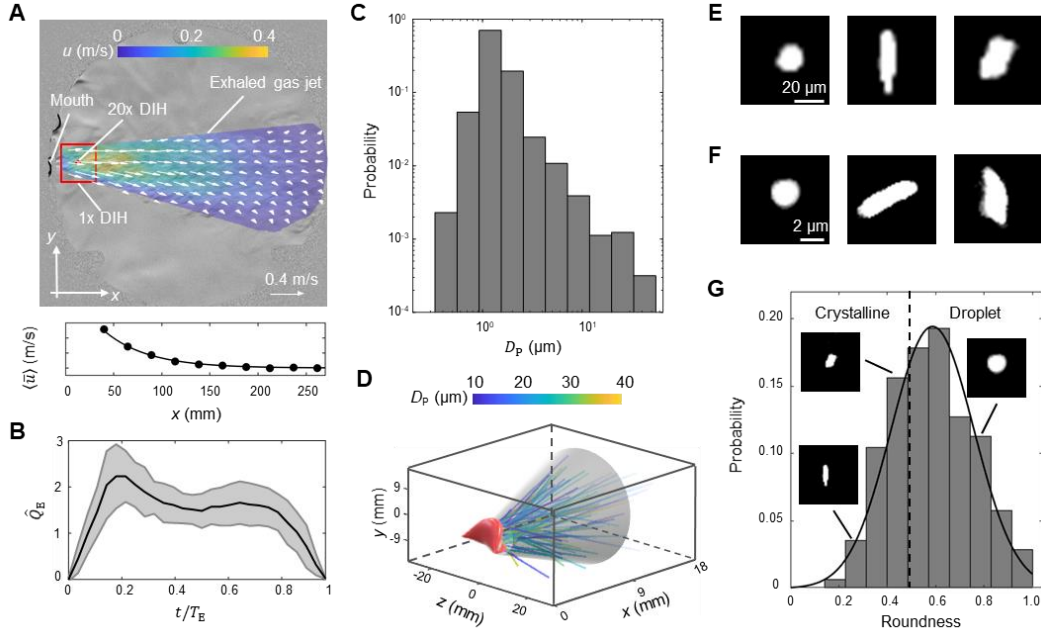


Fig. 1. (A) The ensemble average flow field of exhaled gas of all participants superimposed onto an enhanced Schlieren image sample of exhaled gas flow. The details of generating this figure can be found in the supplementary materials. The locations of the mouth, the sampling windows of 1X and 20X digital inline holography (DIH) are marked in the figure. Additionally, the streamwise velocity averaged over the cross section of the exhalation cone ($\langle \bar{u} \rangle$) is plotted against the streamwise distance to the mouth (x) to show the decay of flow velocity. (B) The change of the normalized exhaled gas flow rate (\hat{Q}_E) in one exhalation cycle of time period T_E , where \hat{Q}_E is the instantaneous exhaled gas flow rate (Q_E) divided by its average for each exhalation cycle. The solid curve and shaded area represent the ensemble average and variance of \hat{Q}_E of all participants, respectively. (C) The histogram of aerosol size quantified using area equivalent diameter (D_p). (D) The 3D trajectories of all the aerosols captured using 1X magnification DIH. Sample images of aerosols from (E) 1X and (F) 20X DIH measurements. (G) The histogram of aerosol shape quantified using particle roundness (Fig. S7 with details in the supplementary materials) with inset figures showing samples of aerosols with different roundness levels. The solid line is the fitted normal distribution and the dashed line corresponds to the roundness of 0.5.

The DIH measurements provide the first detailed characterization of the generation of aerosols during normal breathing in terms of their concentration, size, and shape. The measurements have shown an average concentration of 170 aerosols per liter exhaled gas (i.e., 44 aerosols per breath) from an ensemble average of 160 minutes DIH data from eight participants. The particle size distribution peaks around $1.5 \mu\text{m}$ with a sharp decay towards smaller and larger sizes and an averaged value of $1.7 \mu\text{m}$ (Fig. 1C), which is substantially higher than the $0.6 \mu\text{m}$ obtained from OPC measurement (13) and close to the $2 \mu\text{m}$ measured using microscopic examination of aerosols deposited on a glass slide through an impactor (13). Most aerosols are below $5 \mu\text{m}$ and only 0.2 % above. The 3D trajectories of aerosols ($>5 \mu\text{m}$) within the exhaled gas fit within the breathing cone determined from the Schlieren imaging for all the participants with about 10% aerosols leaking from the side of the mouth occasionally (Fig. 1D). Besides the particle size, the shape of aerosols can be obtained using DIH. Interestingly, in addition to a large fraction of round-shaped aerosols, a substantial fraction yields irregular shapes with edges and corners. Observed both above (Fig. 1E) and below $5 \mu\text{m}$ (Fig. 1F), these two types of aerosols with distinct shapes correspond respectively to the droplets and crystalline aerosols generated from human breathing reported in the literature (13, 24). Particularly, through mass spectra of aerosols, the literature has revealed the presence of nonvolatile solutes such as potassium, calcium, and chorine contents in crystalline

aerosols (13, 24), which are likely to be generated from the alveolar fluid from the lower respiratory tract (12). To quantify the content of aerosols based on their shapes, the histogram of roundness of aerosols (Fig. S7 with details in the supplemental materials), is obtained (Fig. 1G), and a roundness threshold of 0.5 is selected to categorize the aerosols into droplet and crystalline types according to the literature (25, 26). Accordingly, our measurements suggest about 33% of aerosols produced by normal breathing are crystalline type appearing both below and above 5 μm (Fig. S12 shows that aerosol roundness is independent with the size). These crystalline aerosols are usually hygroscopic (24) and could take up moisture from the environment with increasing humidity to form droplets up to 2.5 times their original sizes (27). It has been suggested moisture can insulate viruses from extreme environments, in favor of their survival during transmission (28). Therefore, these crystalline aerosols could also (in addition to droplets) serve as the virus carriers for airborne transmission.

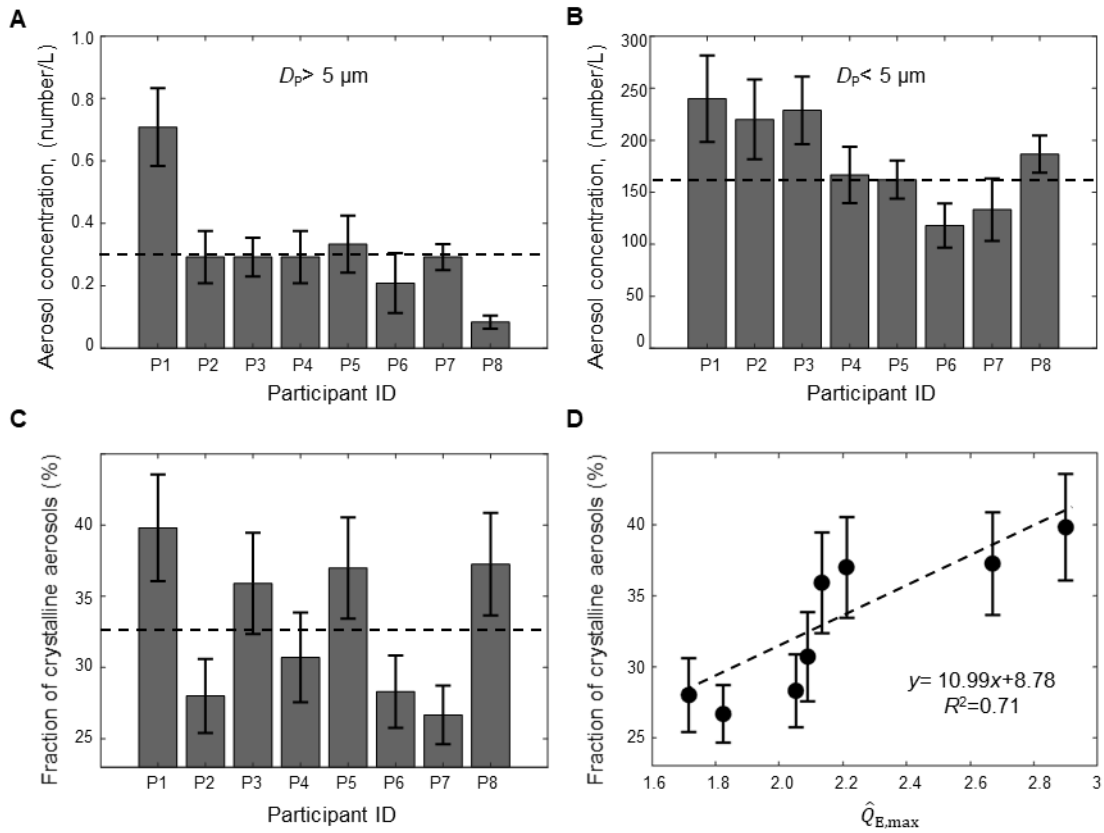
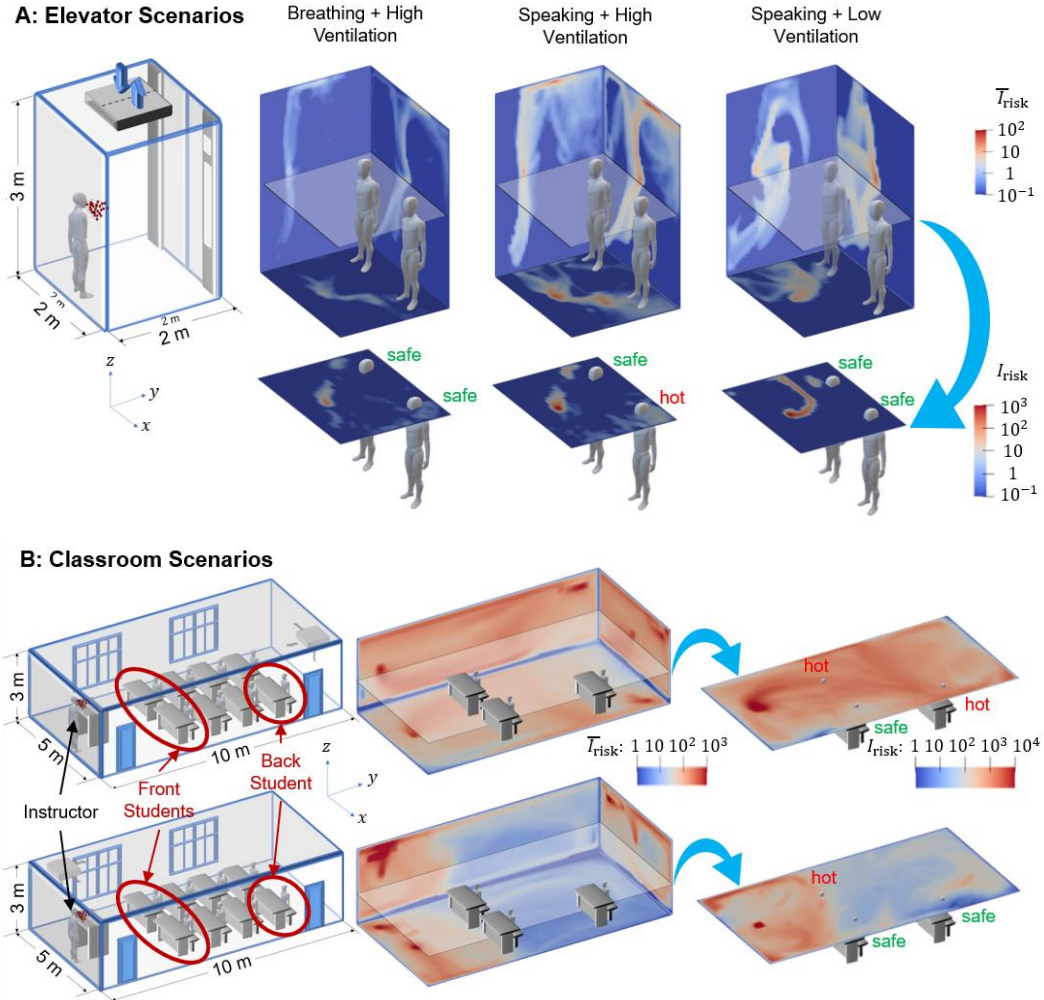


Fig. 2. The variation of aerosol concentration (number/L) across different participants for (A) aerosols larger than 5 μm and (B) smaller than 5 μm . The dashed lines in the figures correspond to the average aerosol concentration. (C) The variation of the fraction of crystalline aerosols across different participants with its average value marked by the dashed line in the figure. (D) The variation of the fraction of crystalline aerosols with respect to the normalized peak exhaled gas flow rate ($\hat{Q}_{E,\text{max}}$) of each participant. The dashed line and the equation in the figure are the least square linear fit of the data.

The aerosol measurements exhibit interesting variability across different participants using the same normal breathing techniques (Fig. 2). Specifically, the concentration of aerosols larger than 5 μm varies significantly across different individuals (Fig. 2A) while the aerosols smaller than 5 μm do not show such large variation (Fig. 2B). In particular, the concentration of aerosols larger than 5 μm produced by one participant (P1) is more than twice the average concentration of the

eight participants. Considering aerosols in this scale range contain higher viral loads (29, 30) and can evaporate rapidly to be airborne, such an individual can be more effective in spreading viruses when asymptomatic. It is worth noting that other studies on aerosol generation during breathing and speaking also reported the presence of such superemitters, with population percentage ranging from 6% to 25% (12, 31), consistent with the percentage of such individual (12.5%) observed in our experiments. Superemitters of aerosols have been related to the superspreaders of infectious diseases in the literature (10, 31, 32). Remarkably, the percentage of superemitters in our study (though there is large uncertainty due to the small sample size) coincides well with the 10% of superspreading events of COVID-19 observed in preliminary clinical data (33), providing further support to the spreading of COVID-19 through aerosol generation from asymptomatic individuals. In addition, the fraction of crystalline aerosols varies from 26% to 40% across different participants (Fig. 2C), and shows a strong correlation with the peak of normalized exhaled flow rate ($\hat{Q}_{E,max}$) defined earlier (Fig. 2D). Considering the connection between $\hat{Q}_{E,max}$ and the natural breathing depth of individuals as noted earlier (21-23), our results provide strong evidence that the deeper exhalation can lead to the generation of a higher fraction of crystalline aerosols from the lower respiratory tract as suggested in the literature (12).



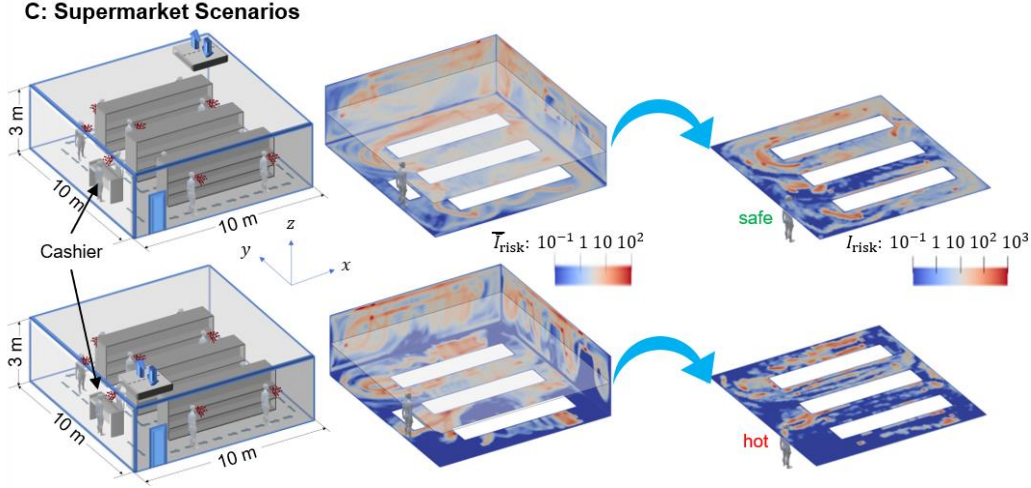


Fig. 3. Numerical simulation of aerosol transport and deposition to evaluate the risk under (A) an elevator setting with a simulated asymptomatic individual breathing under high ventilation of 212 cubic feet per minute (CFM), speaking under high ventilation and low ventilation of 15 CFM, (B) a small classroom setting with a simulated asymptomatic instructor and the ceiling ventilation system located in the back corner and front of the classroom (supplemental video S5), respectively, and (C) a small supermarket setting with a simulated asymptomatic shopper (his/her 10 stops along the dashed route are marked in the schematic) and the ceiling ventilation system located at the back corner and entrance of the supermarket, respectively. Except for the low ventilation setting in A, the ventilation rate of each setting is designed to replace all the air in the space every two minutes, representing the upper bound recommended ventilation condition in current systems. Under each setting, the risk of a person encountering virus-containing aerosols at one specific location (I_{risk}) is evaluated as the total aerosol number passing through this location during the simulation time, which can be interpreted as how many aerosols a person can inhale at this location during the simulated time. Note that such an estimate of the inhaled aerosol number only provides an upper estimate of aerosol encounter since it does not consider the detailed flow processes involved in the inhalation of aerosols. In the 3D contour plots, the wall contours are the contours of I_{risk} spatially averaged (denoted as \bar{I}_{risk}) along x , y , and z directions, respectively. In addition, assuming the height of each individual is ~ 1.75 m, selected horizontal slices of I_{risk} contour at the height of human mouth are highlighted to show the I_{risk} for individuals standing (1.6 m for A and C) or sitting (1.2 m for B) at different locations, and several representative locations are marked as safe or hot based on their I_{risk} values (safe criterion: $I_{\text{risk}} \leq 1$ for A; $I_{\text{risk}} \leq 200$ for B; $I_{\text{risk}} \leq 100$ for C).

Using the flow and aerosol information derived from our breathing experiments, numerical simulations are conducted under three practical settings to determine the aerosol transport and deposition and assess the risk of being infected I_{risk} through the airborne transmission of COVID-19 caused by asymptomatic individuals (Method Section in supplemental materials).

Under the elevator setting (Fig. 3A), a simulated asymptomatic individual (referred to as the “emitter” hereafter) is placed near the wall opposite to the door for one minute. With high ventilation, the aerosols from the emitter disperse to a large portion of the elevator within one minute, but I_{risk} is extremely low (≤ 1) in most of the space (e.g., the two “safe” spots). To assess a riskier scenario, we consider the emitter speaking continuously for one minute and producing aerosols at a rate 10 times that of normal breathing according to the literature (2, 4). Without changing ventilation, this scenario exhibits a proportional increase in I_{risk} and the expansion of regions with high risks (e.g., the “hot” spot). With significant reduction in ventilation, the dispersion of aerosols is confined to one quadrant of the elevator on the emitter side, imposing little risk to people who are not standing in close proximity to the emitter (e.g., in the two “safe” spots) but two orders of magnitude higher risks for some local hot spots in the quadrant. Remarkably, even under high ventilation, only a small fraction ($\sim 15\%$) of aerosols is vented out, and the number drops to zero with reduced ventilation. This observation is associated with the

presence of stable flow circulation zones in the space (Fig. S13), which traps the aerosols and increases their residence time to be significantly longer than the simulated time here. In addition, such circulation zone strengthens with increasing ventilation causing more wall deposition of aerosols (Fig. S16).

Under the small classroom setting (Fig. 3B), we consider the emitter to be the instructor upfront and the aerosols are continuously produced through speaking for 50 minutes (the typical duration of a lecture), representing a much riskier scenario in comparison to one of the breathing students being the emitter. When the ceiling ventilation is at the back corner in the classroom (i.e., far from the emitter), the ventilation spreads aerosols to the back half of the classroom. Particularly, the region near the vent can yield a significantly higher I_{risk} , such that a student sitting in a hot spot in the back could inhale several times more aerosols than a front student at a safe spot. As the ventilation is relocated to the emitter side, the spread of aerosols is mostly confined to the region before the front students and the I_{risk} for each student is significantly reduced compared to the former scenario. Remarkably, despite the rate of ventilation set to replace all the air in the space every two minutes for both scenarios, no more than 10% of the total emitted aerosols are vented out after 50 minutes, although the latter (i.e., ventilation near the emitter) doubles the fraction of vented-out aerosols of the former (Table S2). Such inefficient aerosol removal through ventilation is largely associated with the presence of many stable circulation regions in the large space (Fig. S14), which increases aerosol residence time, causes the majority of aerosols deposited to surfaces (i.e., 88% of the total, Table S2), and forms hot spots of surface contamination (e.g., the two ground corners on the same side of the classroom for both ventilation scenarios, Fig. S17).

Under a small supermarket setting (Fig. 3C), the emitter is considered as an asymptomatic shopper with regular breathing, who makes 10 stops (three minutes for each stop with the last stop at the cashier) along a designated zigzag shopping path for 30 minutes. When the ceiling ventilation is in the back corner, the aerosols spread across the entire supermarket, and particularly, a hot spot is formed in the space between the leftmost shelf and corner near the ventilation due to strong local circulation and entrainment of higher speed channeling flow formed in this space (Fig. S15). However, the cashier, standing near the entrance, is placed in a relatively safe zone. With the ventilation moved to the entrance, the overall spread of aerosols is reduced, but several other hot spots emerge, including one in front of the cashier increasing his/her risk by about two orders of magnitude. Compared with the classroom setting, the fraction of vented-out aerosols (~50% for both scenarios, Table S2) is significantly increased here, even at similar ventilation and shorter time duration. Such increase in the aerosol removal efficiency is primarily attributed to the motion of the emitter which limits the chance of a large fraction of aerosols becoming trapped in the same stable circulations. Additionally, due to the presence of dividing structures (i.e., shelves), the stable circulation zones reduce in scale (Fig. S15) in comparison to those under the classroom setting, causing less wall deposition except in the back corner near the ventilation (Fig. S18).

Combining novel *in situ* measurements and simulation, our study provides the first quantitative assessment of risks due to airborne transmission of viruses generated by asymptomatic individuals in a confined space under ventilation. Our results show significant spatial heterogeneity of risks in confined spaces under three practical settings, supporting the interesting observations of COVID-19 infection associated with air conditioning in a restaurant (44). Specifically, although ventilation enables the removal of virus-containing aerosols, it can help spread aerosols to larger spaces beyond the proximity of asymptomatic individuals. Inappropriate ventilation can also lead to local hot spots with risks that are orders of magnitude higher than other places depending on the relative

positioning of aerosol emitter, ventilation, and space settings. In addition, ventilation can also enhance aerosol deposition on surfaces causing patched regions with high surface contamination, consistent with the large amount SARS-CoV-2 RNAs extracted from samples collected from hospital floors and air vents (34, 35). Particularly, ventilation at a single location, even at the highest rate in the current practice, is **highly inefficient** at removing aerosols, due to the presence of relatively stable flow circulation zones in the space and the large amount of aerosol deposition on surfaces. This result suggests that improvements to air filters alone are not enough to reduce the aerosol concentration.

Our study can directly lead to practical guidelines and science-driven policy for mitigating the risks of airborne infection of COVID-19 with minimal impact on the economy and social activities, which are critical for the safe re-opening of many businesses. Specifically, our results suggest that optimizing ventilation settings (e.g., adding more sites of ventilation and/or more turbulence to disrupt stable circulation zones) even under the current ventilation capacity can significantly improve the efficiency of aerosol removal. Adjusting the placement of occupants (e.g., students or cashier in our cases) in the room to avoid hot spots and frequent cleaning of surfaces prone to contamination can reduce the risks. Wearing masks to cut down the source of aerosol generation can significantly lower the risks of airborne infection. Additionally, our *in situ* characterization of aerosol generation through breathing shows its large variability and correlation with individual breathing depth, indicating the need for effective risk assessment at an individual level. Our study can be further extended to a broad range of practical settings (e.g., air cabin, restaurant, gym, etc.) with more detailed physics (e.g., exhalation, inhalation flow physics, etc.) and individual characteristics (e.g., exhalation behavior, movement, etc.) as well as more precise HAVC models incorporated to yield more accurate risk assessment under these settings.

Supplementary Materials:

1. Experimental methods

1.1 Participants

Eight healthy participants including five males and three females, and age ranging from 21 to 29. The University of Minnesota Institutional Review Board (UMN IRB) approved this study (NO:00009795), and all research was performed in accordance with the relevant guidelines and regulations of the UMN IRB. Written informed consent was obtained from all participants prior to the study participation and all the participants completed a brief questionnaire including their age, gender, and healthy conditions.

1.2 Breathing patterns

The rate of participant breathing is set at values that have been identified as normal for healthy individuals (36). The breathing rate is set with the aid of a metronome operating at 76 beats per minute. The nose inhale lasts for 2 beats (1.58 s) while the mouth exhale lasts for 3 beats (2.37 s). A mouthpiece consisting of a 2.0 cm hole in a 6 mm thick acrylic plate is used to align the participant's mouth with the imaging volume. The participant's head position and the dimension of the mouthpiece are shown as Fig. S1. Before the experiments, a presentation describing the detailed breathing techniques was sent to the participants for them to practice the breathing techniques. During the experiments, the participants were instructed to adjust their breathing patterns according to the live view of the Schlieren imaging. This same breathing technique is used for each of the subsequent measurement methods.

1.3 Schlieren Imaging

Schlieren imaging is a technique that visualizes the index of refraction variation within a fluid that can be caused by variations in temperature, pressure, or composition (37). Schlieren imaging has previously been used to characterize exhalation (38) and study airflow patterns with and without a facial mask (39). The components in the high-speed Schlieren imaging system are shown in Fig. S2. It consists of a blue fiber-coupled LED light source, a concave mirror (30.5 cm diameter, 2.3 m focal length), a blade, and a camera (NAC Memrecam HX-5) with imaging lens (Nikon AF Nikkor 80-200 mm 1:2.8 D). The image size is 960×936 pixels (32×32 cm field of view) and is recorded at 1000 Hz with a $100 \mu\text{s}$ exposure time. Each participant takes five breaths for a duration of 20 s. The time-resolved standard deviation of pixel intensity of the Schlieren sequence corresponding to each participant is used to determine the geometry of the exhaled gas jet (i.e., breathing cone angle, shown as Fig. S3). We use optical flow to quantify the flow field, using open source software developed by Liu et al (40), with a 5-frame skip to ensure sufficient displacement of flow structures inside the exhalation cone. The interrogation window is chosen as 32×32 pixels. The flow field is subsequently used to determine the volumetric flow rate of the exhaled gas jet by integration of the flow velocity over the cross section of the exhalation cone at a fixed location (3 cm downstream of the mouthpiece), assuming the jet is axisymmetric. For the ensembled average flow field of the breathing (Fig. 1A in the main text), the averaged flow field of 20 Schlieren video frames around the $0.2T_E$ of each breath was taken first. Then, the flow fields of 40 breaths of all the participants are realigned to a specific breathing cone captured from participant 2 and ensembled to have the averaged flow field shown as the Fig. 1A. Fig. S4 shows the breathing patterns of all participants observed in the present study. Note that despite similar patterns of breathing, the normalized peak exhaled gas flow rate varies substantially across the participants.

Table S1 is a summary of the Schlieren results of all the participants including their average exhaled gas flow rate and the breathing cone angle.

1.4 1X magnification digital inline holography (DIH) measurements

DIH is an optical diagnostic technique which allows *in situ* imaging of individual microparticles in an extended sample volume (i.e., orders of magnitude larger than conventional microscopy in the imaging depth of field) without focusing (41-43). DIH operates using the principle of optical diffraction; spatially and temporally coherent reference light beam illuminates the sample (aerosols). Light scattered by the aerosols interferes with the unscattered portion of the reference beam. The recorded diffraction pattern (or hologram) can be digitally refocused through convolution with a diffraction kernel, to determine the size, shape, location, and optical properties of the aerosols. Two magnifications are used to increase the measured size range. The 1X magnification digital inline holographic imaging (DIH) system is used to image exhaled aerosols ranging in size primarily from 10 μm to 50 μm . Our 1X DIH system, shown in Fig. S5, consists of a He-Ne laser, a spatial filter (Newport Inc) and a collimation lens ($f=45\text{ mm}$) producing a 2 cm diameter gaussian beam. A large format CMOS camera (4000 \times 4000 pixels; Viewworks Inc) captures the holograms over a 18 \times 18 mm field of view at a resolution of 4.5 $\mu\text{m}/\text{pixel}$, sampling at 35 frames/s. Since the exhaled jet diameter is 16 mm, the volume containing aerosols is 18 \times 18 \times 16 mm^3 (5 mL). The field of view and center of the laser beam are vertically aligned with the mouthpiece opening and offset by 1.5 cm (see Fig. S6) to ensure the sample volume covers the whole breathing jet at the measurement location. The measurements from each participant are repeated 20 times, with each dataset consisting of a 30 s hologram sequence replicating the breathing technique used in the Schlieren measurements. Hologram processing has three steps. First, the holograms are resized to 1024 \times 1024 pixels to reduce processing time and enhanced by time averaged background division to remove stationary artifacts present in the image and remove spatial intensity variations. Then, the holograms are reconstructed by convolution with Rayleigh Sommerfeld diffraction kernel (42) to obtain a 3D optical field. Such 3D optical field is used to determine the rough 3D centroids of the exhaled aerosols. The original size (4000 \times 4000 pixels) holograms containing particles are reconstructed near the rough longitudinal location determined from the first step to get the precise longitudinal planes of the aerosols. The background particles, i.e., particles captured by the DIH system between consecutive exhalations of the participants, consist of about 15 % of the total particles captured by the DIH. We combined three criteria to distinguish the exhaled aerosols from the background particles. First, the aerosols have a streamwise speed from 0.1 to 0.3 m/s near the DIH measurement window according to Schlieren measurements. Second, the initial z locations (longitudinal) of the aerosols are restricted between -8 mm and +8 mm to the mouth, which overlaps with the position of the jet from the image plane. Third, the aerosol trajectories generally follow the exhaled cone shape established from the Schlieren measurements. The aerosol size and shape are manually measured from 100 \times 100 pixels cropped images using ImageJ. We use the area-equivalent diameter D_p (Eqn. 1) to quantify the aerosol size and use roundness (Eqn. 2) as a measure of aerosol shape. The cross sectional area and the major axis length of the aerosols are given by A and D_{maj} , respectively, where the latter is determined by an ellipse fit (a few samples are shown in Fig. S7).

$$D_p = \sqrt{4A\pi} \quad (1)$$

$$\text{Roundness} = 4A/(\pi D_{\text{maj}}^2) \quad (2)$$

1.5 20X magnification DIH measurements

We modify the 1X DIH imaging system by introducing a 20X microscopic objective (Mitutoyo Plan Apo 20X, 0.42 NA) and replacing the spatial filter by a 4X objective lens for reducing the beam expansion to 3 mm from 2 cm. The camera provides an imaging resolution is 0.23 $\mu\text{m}/\text{pixel}$ resulting in a sample volume of $0.9 \times 0.9 \times 4 \text{ mm}^3$ ($2.0 \times 10^{-4} \text{ mL}$). The individual components and participant head position for the 20X DIH measurements are shown as Fig. S8 and Fig. S9, respectively. The sample volume reduced depth is due to the laser beam energy loss due to the higher magnification of the objective lens. The system is capable of resolving aerosols that are around 0.5 μm very accurately. Similar to the 1X data acquisition, the 20X experiments consist of 20 repetitions with each participant, generating 30 s of data each. Once recorded, the holograms are processed following the same algorithm described above for the 1X DIH measurements.

1.6 Combining 1X and 20X DIH measurements

To compare the total concentration of the aerosols measured by both systems, we multiply the volume-averaged count by the ratio of the volumes for both measurements with the assumption that the aerosols are uniformly distributed in the breathing jet (schematic shown as Fig. S10). We further confirmed such assumptions by plotting out the initial y (vertical) and z (longitudinal) locations of the aerosols captured from 1X DIH measurements (Fig. S11). Lastly, the particle roundness and particle size are independent with each other as shown in Fig. S12.

2. Numerical Simulation

The simulations are conducted based on the OpenFOAM-6 platform, with the Eulerian-Lagrangian framework for the gas-liquid phase simulation. The gas phase flow is governed by a set of conservation equations:

$$\frac{\partial \rho_g}{\partial t} + \nabla \cdot (\rho_g \mathbf{u}_g) = \dot{S}_m \quad (3)$$

$$\frac{\partial \rho_g \mathbf{u}_g}{\partial t} + \nabla \cdot (\rho_g \mathbf{u}_g \otimes \mathbf{u}_g) = -\nabla \rho_g + \nabla \cdot \boldsymbol{\tau}_g + \dot{S}_F \quad (4)$$

where t is time, ρ_g is the density of the gas mixture, subscripts g indicates the gas phase, \mathbf{u}_g is the velocity vector including velocities in three directions. $\boldsymbol{\tau}_g$ is the viscous stress tensor. \dot{S}_m and \dot{S}_F are the source terms incurred by the Lagrangian particles, which are calculated by:

$$\dot{S}_m = \frac{1}{V_{\text{cell}}} \sum_i \dot{m}_{i,d} \quad (5)$$

$$\dot{S}_F = -\frac{1}{V_{\text{cell}}} \sum_i \mathbf{F}_{i,d} \quad (6)$$

where the summation over i means the summation over all the Lagrangian particles, $\dot{m}_{i,d}$ is the rate of change in mass of a particular Lagrangian particle, $\mathbf{F}_{i,d}$ is the drag force of the Lagrangian particles. The dispersed liquid phase is modeled by a large number of spherical droplets tracked by a Lagrangian model. Due to the small size of the aerosol in this study, the primary break-up is neglected. In addition, the spray is assumed to be diluted and hence, the interactions between Lagrangian particles are also ignored. The mass rate of change $\dot{m}_{i,d}$ and the drag force $\mathbf{F}_{i,d}$ govern the dynamics of each Lagrangian particle by:

$$\frac{dm_{i,d}}{dt} = \dot{m}_{i,d} \quad (7)$$

$$\frac{du_{i,d}}{dt} = \frac{F_{i,d}}{m_{i,d}} \quad (8)$$

Only the Stokes drag is considered for the drag force, which is detailed in (44). Considering the room temperature and 40% humidity in this study, the classical evaporation model based on quasi-steady-state assumption is used to account for the evaporation because the temperature is reasonably far from the boiling point (45). The mass rate of change by evaporation is calculated by:

$$\frac{dm_d}{dt} = \rho_d \pi d_d \cdot Sh \cdot D_i \ln \left(\frac{1 - X_{i,c}}{1 - X_{i,s}} \right) \quad (9)$$

where d_d is the diameter of the droplet, $X_{i,c}$ is the surrounding carrier phase (air in this study) concentration. $X_{i,s}$ is the concentration at the surface of the Lagrangian particle calculated by Raoult's law:

$$X_{i,s} = \frac{X_i p_{sat,i}}{p_c} \quad (10)$$

where p_c is the surrounding pressure approximated by the same method as $X_{i,c}$ and $p_{sat,i}$ is the saturation pressure of the liquid phase (water in this study). Sh is the Sherwood number and D_i is the vapor diffusivity. The Sherwood number and diffusivity are calculated by the Ranz-Marshall model (45). All the gas phase differential equations in this section are discretized and numerically solved with the finite volume method based on the OpenFOAM-6 platform (46).

2.1 Ventilation

In three different practical settings (confined spaces including elevator, classroom and supermarket), ventilation is considered as inlet and outlet boundaries in the simulations, which replace the air in the confined space with constant air entrance and exit flow rates.

The ventilation of the elevator case is located at the top, consisting of two adjacent faces with one as the inlet and the other one as the outlet. Then vent area of the inlet is 0.5 m². According to the elevator air conditioner ventilation standard in (47), we consider replacing all the air in the elevator every 2 minutes, which corresponds to a high ventilation flow rate of 212 cubic feet per minute (CFM). As a comparison, the low ventilation case uses 15 CFM as the ventilation flow rate, following the 1970s elevator ventilation standard (48).

For the classroom case, a box-like air conditioner with a size 1 × 1 × 0.5 m³ (the vertical height is 0.5 m) is located at one corner of the domain. Three faces of the air conditioner are attached to the wall, while the other three faces, with the bottom as the outlet and the other two side faces as the inlet, are imposed with fixed value boundary conditions. The ventilation air flow rate is set as 1615 CFM, based on the standard in (49).

In the supermarket case, two scenarios with different ventilation locations are simulated. One location is near the entrance, and another location is in the diagonal corner of the entrance. The ventilation air flow rate is 5297 CFM, corresponding to replacing all the air in the supermarket every two minutes according to (49).

Ventilation in these simulations is supposed to generate recirculation in the domain, which promotes the airborne transmission of the aerosols. Considering the ventilation flow rate and the computational domain size, all the cases reaches “quasi-steady state” before injection by simulating 60 s.

2.2 Injections

The breath frequency, as measured in the experiments, is set as one breath per 4 s. The virus carrier (the liquid parcels) are assumed to be pure water in this study. In the natural breath case, the breath injects aerosols with the frequency of 44 aerosols per breath, while with speaking, the number of aerosols per breath is ten times (440 aerosols per breath) (31). The person who carries the virus is modeled as a Lagrangian particle emitter, spraying Lagrangian particles into the computational domain. In the elevator cases, the emitter is located at (1 m, 0.5 m, 1.6 m) with the injection direction as (0, 1, 0). The breath injection profile is intermittent: during breath inhale, no aerosols are injected. We collected data at one minute, representing the typical time duration that a person could stay in an elevator. In the classroom cases, the person emits aerosols for 50 minutes, with a continuous profile at (2.5 m, 1 m, 1.6 m) with the injection direction as (0, 1, 0), representing the speaking of an instructor for almost 50 minutes of a lecture. In the supermarket cases, to represent a typical shopping-to-cashier path of a customer, ten stops of the injectors are set, each of which injects aerosols for a duration of three minutes by normal breathing. We collected the data at 30 minutes, indicating that the customer has stayed for three minutes at each stop. The last stop at the cashier suggests the checkout and the interaction between the shopper and the cashier.

The injected Lagrangian particles are tracked by the model described in the previous section. We consider a special treatment for the Lagrangian evaporation effect. When the aerosol particle size is smaller than 1.5 μm , the evaporation effect is switched off, indicating the airborne transmission of the virus in dry/crystallized aerosol particles (50). The injected Lagrangian particles are initialized with a size distribution following our experimental measurements.

2.3 Local aerosol number counting

To illustrate the hot and safe zones in different practical settings and quantify the risk of a person encountering virus-containing aerosols (I_{risk}) at different locations, we defined an accumulated aerosol number to represent the number of aerosols that went through a specific location:

$$P(\mathbf{x}) = \sum P_i(\mathbf{x}) \quad (11)$$

where P is the accumulated aerosol number, which is a function of the spatial coordinates \mathbf{x} . To avoid double counting, P_i is defined as:

$$P_i(\mathbf{x}) = \begin{cases} 1, & i \text{ the first time aerosol } i \text{ appears at location } \mathbf{x} \\ 0, & \text{otherwise} \end{cases} \quad (12)$$

As seen, P represents the total number of the aerosol passing through a specified location during the whole simulation period. For better interpretation of the spatial distribution of P , spatial average values in each dimension are calculated by:

$$P_x(y, z) = \int_{x_{\min}}^{x_{\max}} P(\mathbf{x}) dx / (x_{\max} - x_{\min}) \quad (13)$$

$$P_y(x, z) = \int_{y_{\min}}^{y_{\max}} P(\mathbf{x}) dy / (y_{\max} - y_{\min}) \quad (14)$$

$$P_z(x, y) = \int_{z_{\min}}^{z_{\max}} P(x) dz / (z_{\max} - z_{\min}) \quad (15)$$

2.4 Discussions about flow streamlines

The flow fields with the high ventilation (212 CFM) and low ventilation (15 CFM) flow rate in the elevator are characterized by the velocity streamlines, as shown in Fig. S13. The flow field traps the aerosols in the recirculation zone, and drives them close to the wall. These aerosols have a long residence time near the wall, which increases the change of wall deposition. No recirculation zone is formed with the low ventilation rate of 15 CFM near the roof and thus, most of the aerosol particles are deposited on the wall by the large recirculation zone near the emitter height, without any aerosols being removed. By contrast, the high ventilation flow rate of 212 CFM is able to suck aerosol to the top (roof). In the classroom case (shown in Fig. S14), the near-instructor ventilation generates a strong recirculation zone near the instructor and keeps the aerosol from spreading to the far end of the classroom. As a comparison, the far-end ventilation creates a large recirculation throughout the whole classroom, driving the aerosols to spread to the wall and to the far end of the classroom. In the supermarket case (shown in Fig. S15), the valley effect below the far-end (from entrance) ventilation generates a high flow velocity and sucks most of aerosol particles to the near-field below the ventilation. However, in the near-entrance ventilation scenario, the aerosols injected at the first several stops are pulled to the cashier, leading to larger danger of aerosol encounter (i.e., higher I_{risk}). In addition, gas flow velocity magnitude when the ventilation is at the far corner is larger than the velocity magnitude when the ventilation is near the entrance, due to the narrow space between the wall and shopping shelf below the ventilation. This explains the more homogenous aerosol distribution when the ventilation is at the far corner.

2.4 Discussions about wall deposition of aerosols

Compared to the speaking mode, the breathing mode creates less wall deposited aerosols (Fig. S16) due to the lower number of injected aerosols. The same ventilation which creates the same flow field, leads to the same wall aerosol deposition positions on elevator walls. When the ventilation rate is lower, the weak recirculation zone on the top is not capable of spreading the aerosols to different walls. As a result, the designated flow field drives all the aerosols to one wall (i.e., the left wall). In the classroom scenario (Fig. S17), the deposited aerosol numbers are much more than the elevator case, due to continuous speaking of 50 minutes. The comparison between far-end and near-instructor ventilation shows that the near-instructor ventilation keeps the wall aerosols near the speaking instructor, while in the far-end ventilation case, the created recirculation zone deposits the aerosols to all the walls in the classroom. In the supermarket settings (Fig. S18), the far-away ventilation sucks a lot of aerosols to be deposited to the wall near the ventilation, due to the large velocity field below the far ventilation. In the near-entrance ventilation case, the far-end shopper stops inject aerosols and directly deposit to the floor by gravity, due to the weak flow field in the far-end field. The distribution of aerosols (suspended in the air; deposited on the wall; and vented out by the ventilation system) in terms of percentage for each scenario is shown in Table S2.

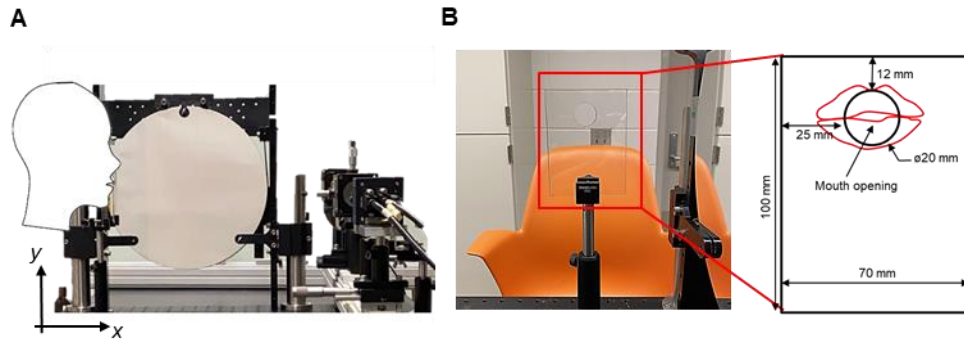


Fig. S1. (A) Image shown the head position of the participants during the experiments and (B) the positioning and dimension of the mouthpiece for aligning the breathing direction of participants.

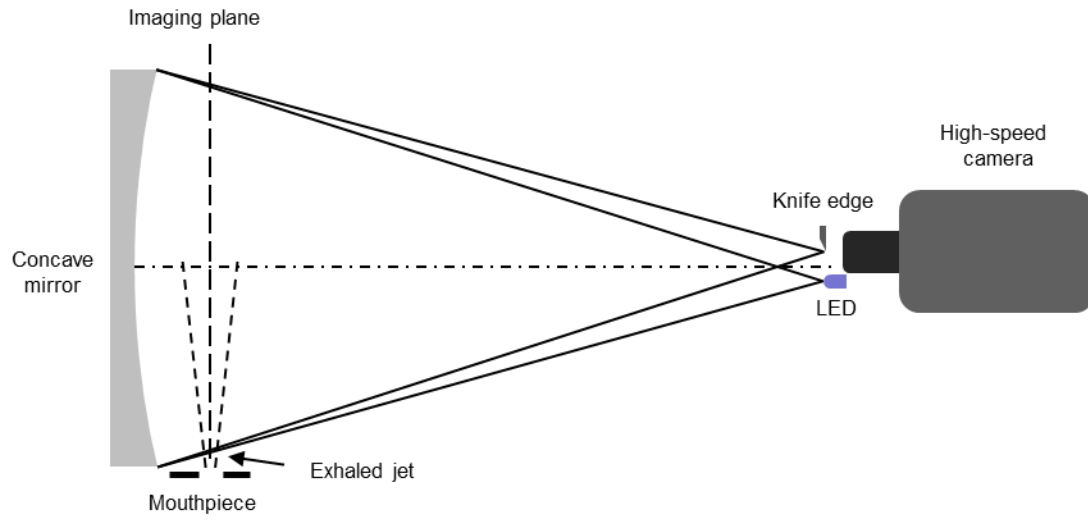


Fig. S2. The high-speed Schlieren imaging system.

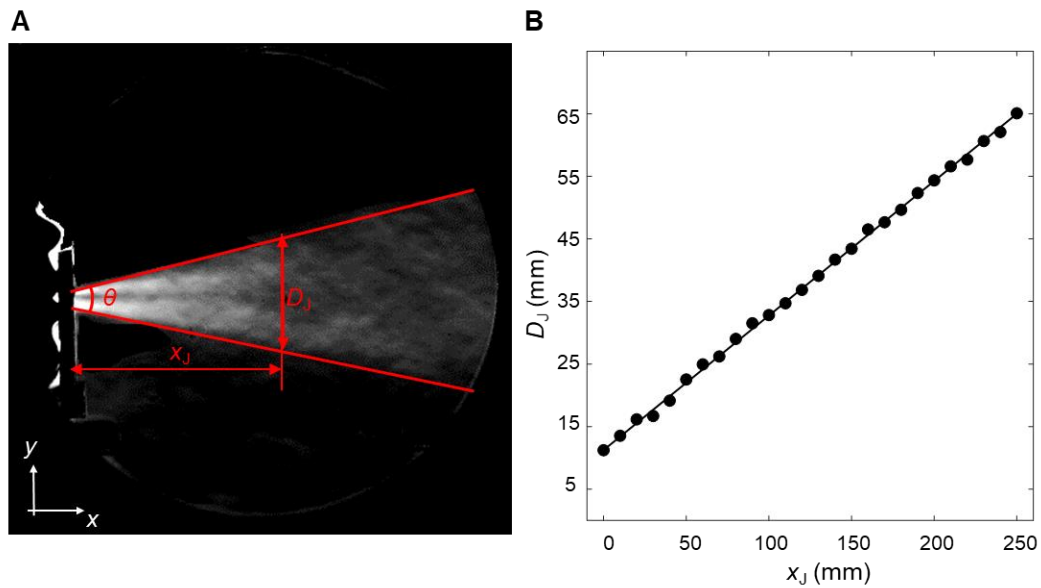


Fig. S3. (A) Standard deviation of all eight participants to show the extent and geometry of the breathing cone, the breathing cone angle θ is used to quantify the breathing cone geometry of each participant and (B) the linear growth of the breathing cone diameter vs. the distance from the mouthpiece.

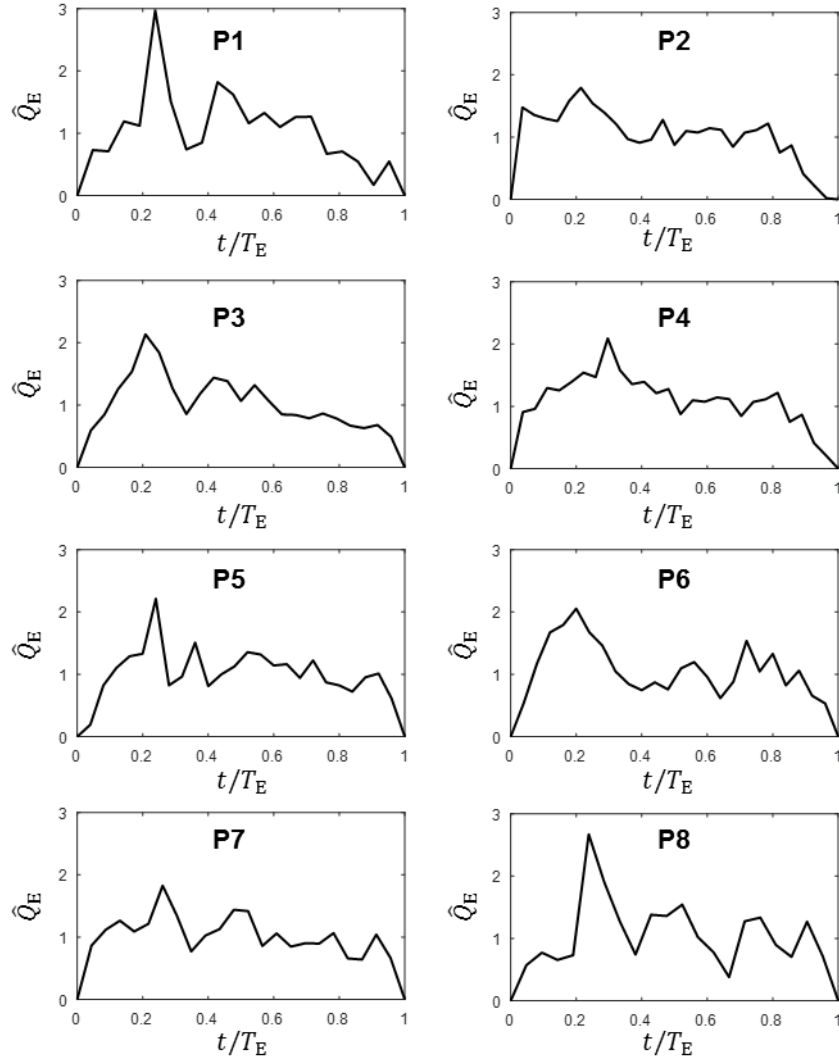


Fig. S4. The instantaneous breathing patterns determined by the normalized exhaled flow rate (\hat{Q}_E) of all participants. The \hat{Q}_E is the instantaneous exhaled gas flow rate (Q_E) divided by its average for each exhalation cycle (T_E).

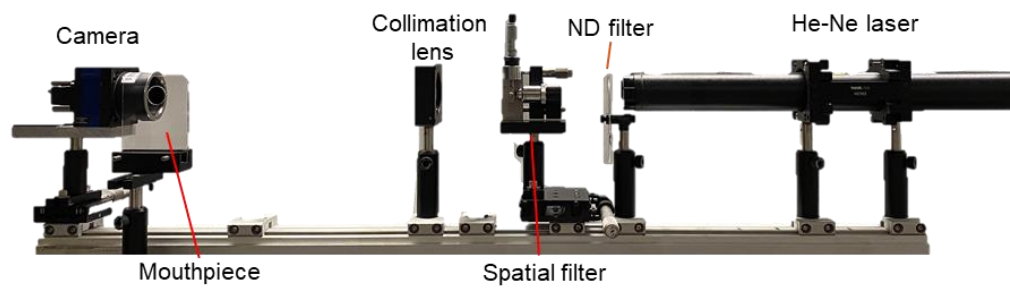


Fig. S5. The components of the 1X DIH measurements.

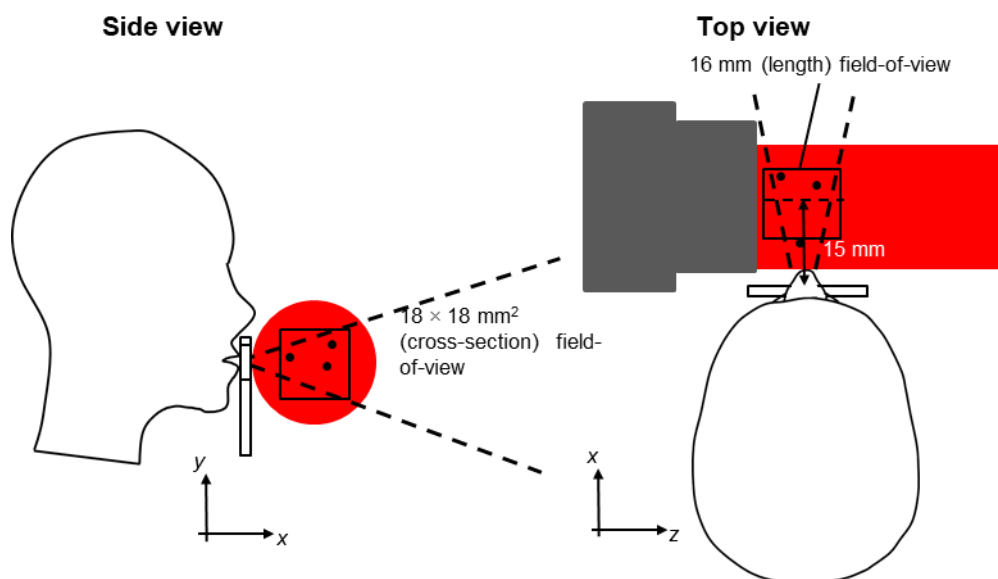


Fig. S6. The schematic shown the side view and the top view of the head position and the measurement window of the participant during the 1X magnification DIH measurements of the exhaled aerosol measurements.

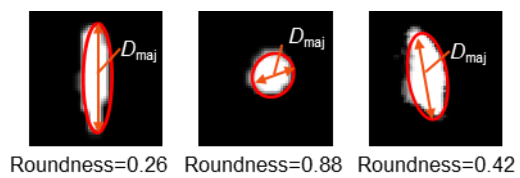


Fig. S7. Sample images show the best fitted ellipses of aerosols their major axis (D_{maj}) used to calculate the roundness of the aerosols.

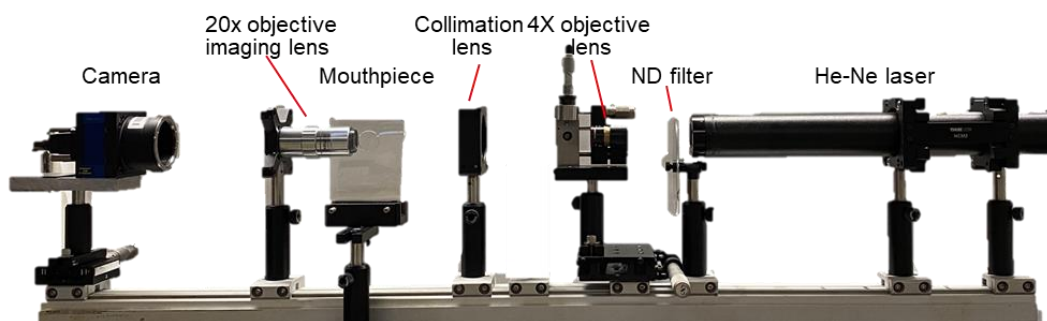


Fig. S8. The components of the 20X DIH measurements.

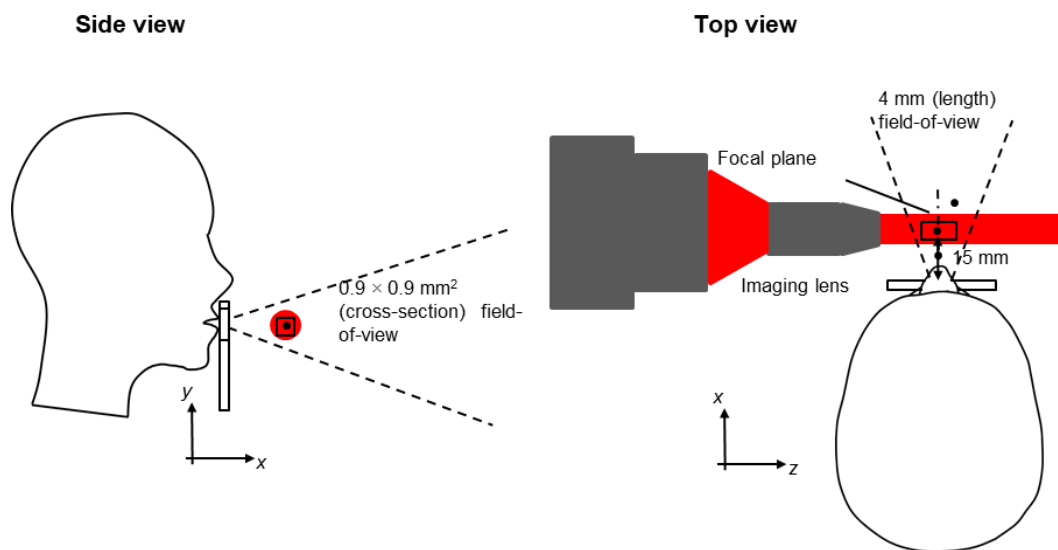


Fig. S9. The schematic shown the side view and the top view of the head position and the measurement window of the participant during the 20X magnification DIH measurements of the exhaled aerosol measurements.

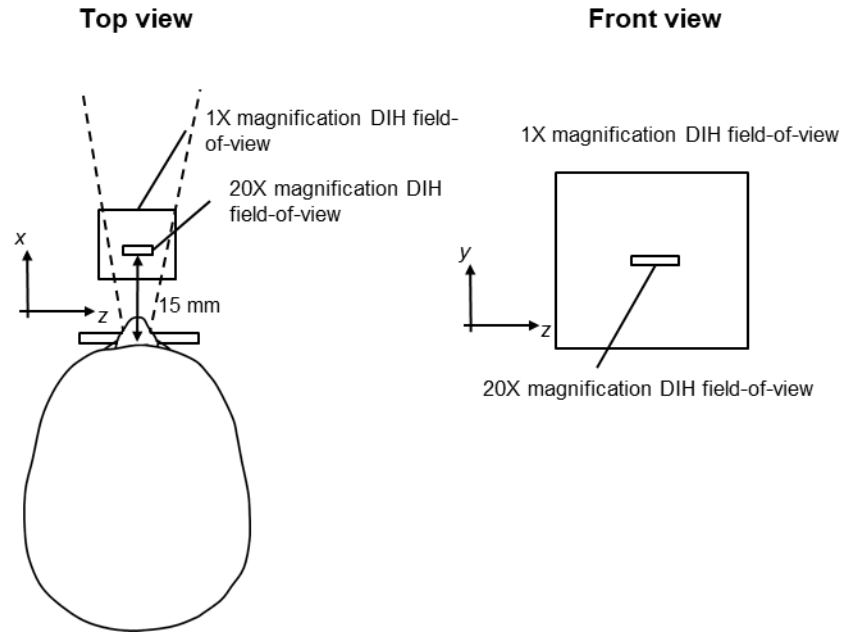


Fig. S10. The schematic shown the top view and the front view of the relative positions of 1X and 20X magnification DIH measurements during the experiments.

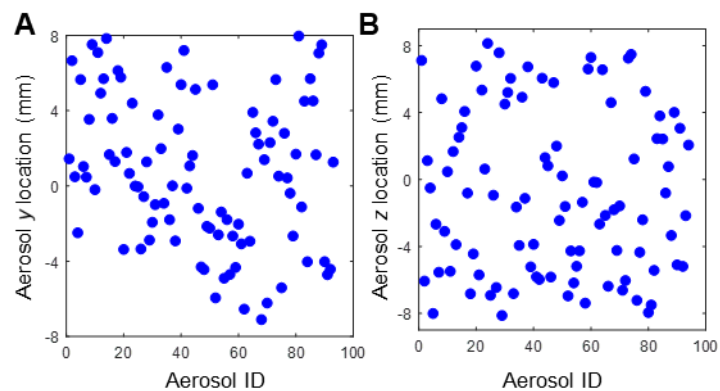


Fig. S11. (A) The y (vertical) location distribution of the aerosols captured in 1X measurement and (B) the z (horizontal) location distribution of the aerosols. The origin of the coordinates is set as the center of the mouthpiece.

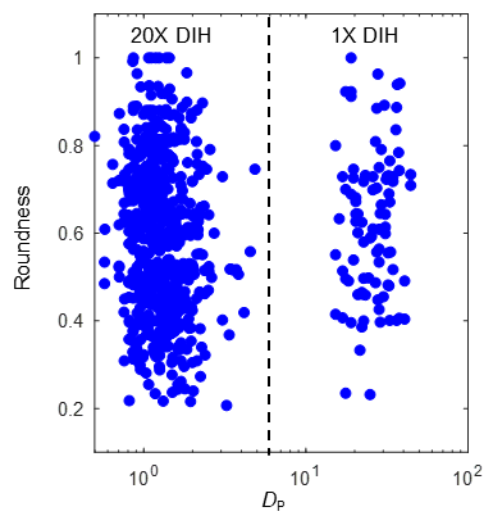


Fig. S12. A scatter plot showing the aerosol roundness versus aerosol area-equivalent diameter (D_p).

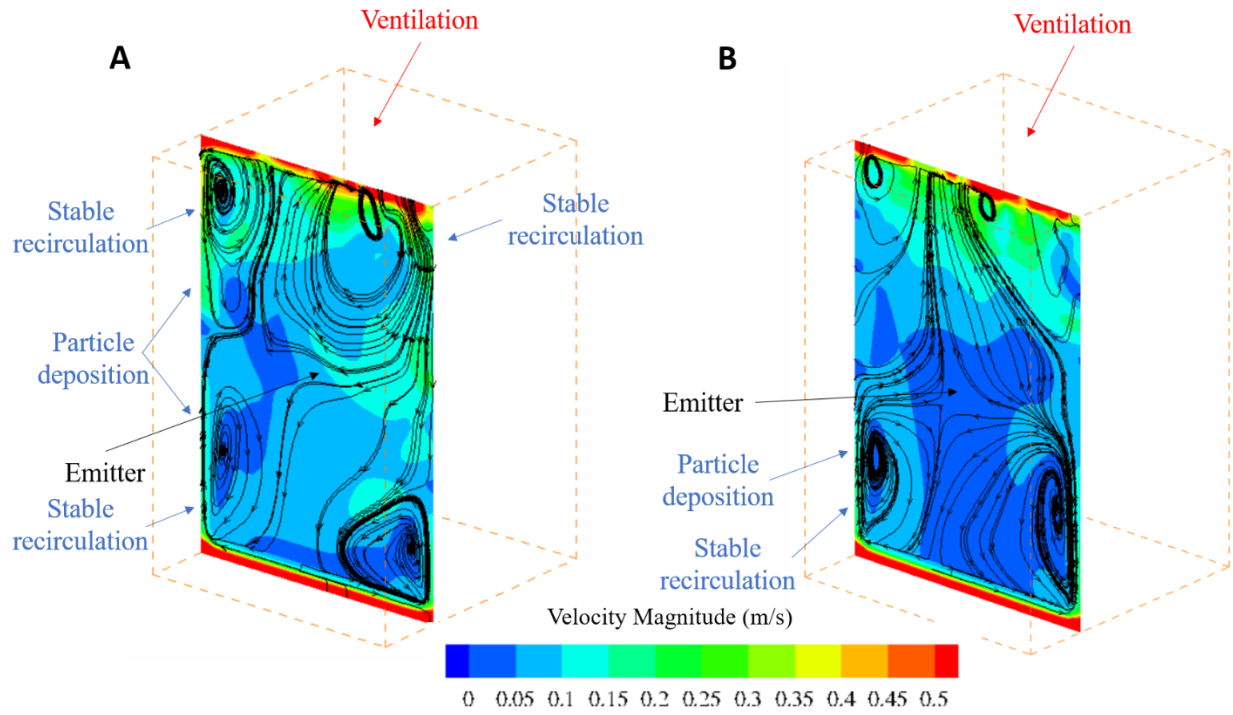


Fig. S13. Velocity magnitude and streamlines on a vertical slice that passes through the emitter for (A) ventilation with the high flow rate of 212 CFM and (B) ventilation with the low flow rate of 15 CFM. For all cases, many particles are trapped in the stable recirculation zones marked in the plots.

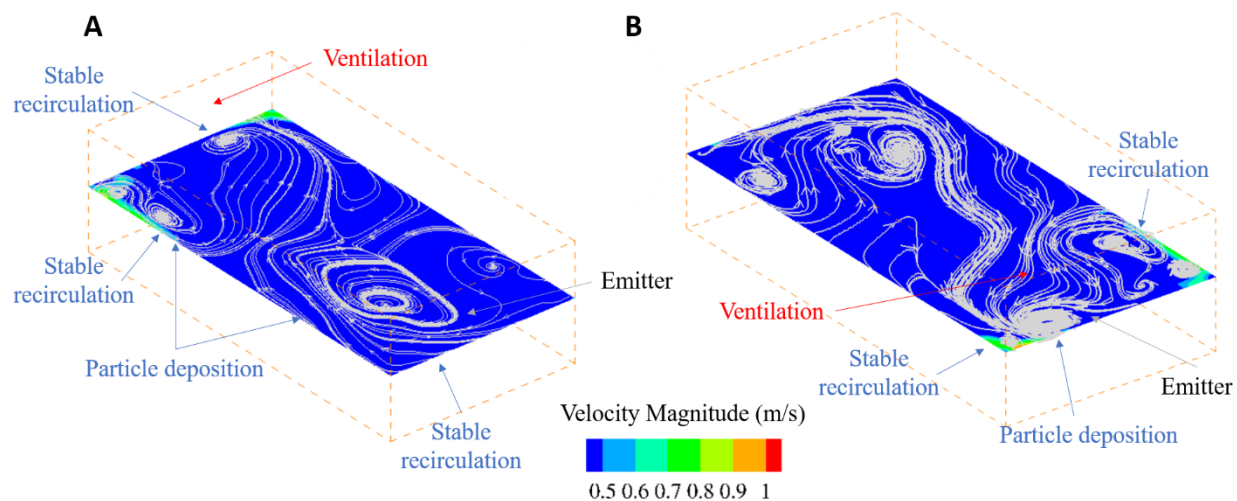


Fig. S14. Velocity magnitude and streamlines at the height of 1.6 m (i.e., the typical height of human noses/mouths) in the classroom cases (**A**) ventilation far away from the emitter (i.e., the instructor) and (**B**) ventilation near the emitter (i.e., the instructor). For both cases, many particles are trapped in the stable recirculation zones marked in the plots.

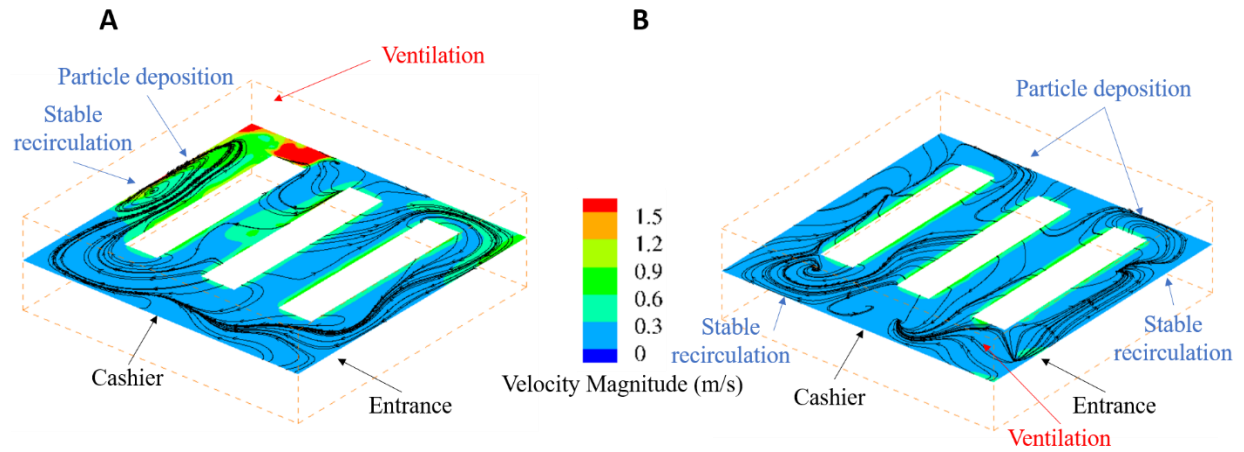


Fig. S15. Velocity magnitude and streamlines at the height of 1.6 m (i.e., the typical height of human noses/mouths) in the supermarket cases (A) ventilation far away from the entrance and (B) ventilation near the entrance. For both cases, many particles are trapped in the stable recirculation zones marked in the plots.

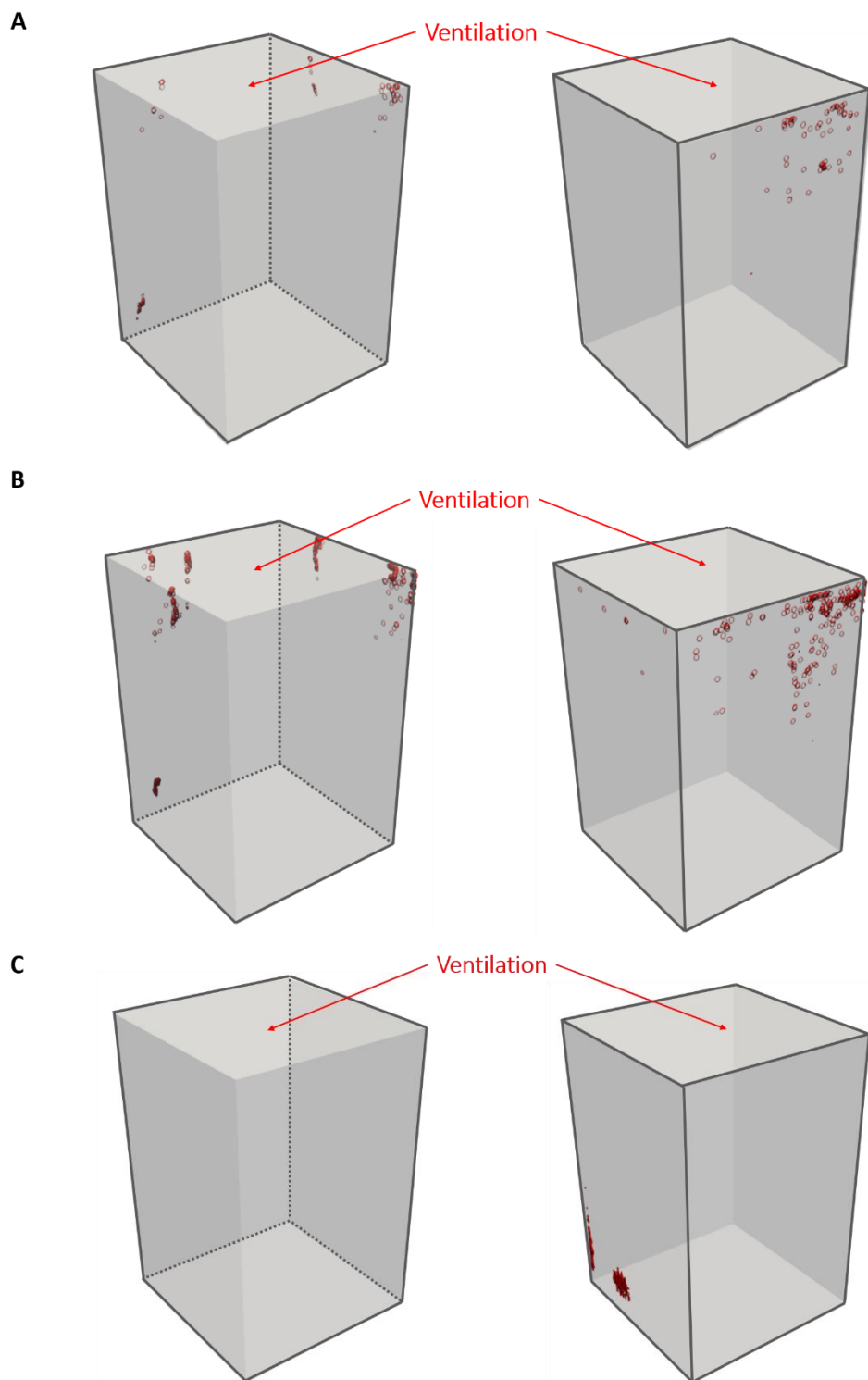


Fig. S16. Aerosol deposition on elevator walls for (A) breathing with high ventilation of 212 CFM, (B) speaking with high ventilation of 212 CFM, and (C) speaking with low ventilation of 15 CFM. For each case, the left subfigure shows the bottom and two inner side walls, and the right subfigure shows the top and two outer side walls.

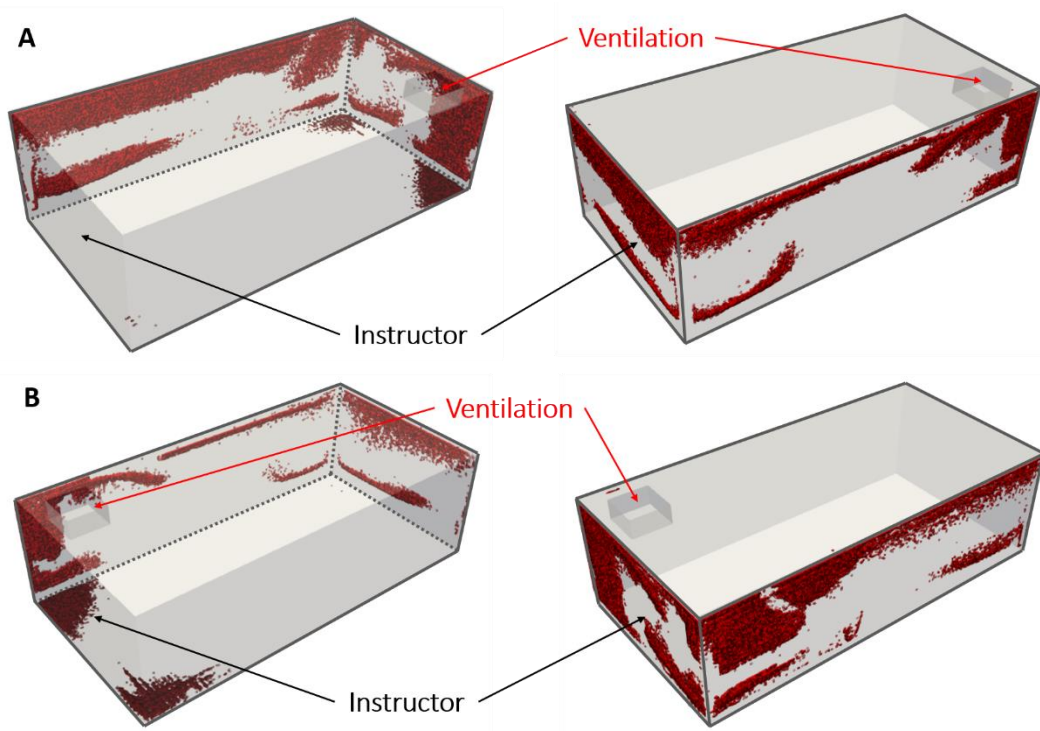


Fig. S17. Aerosol deposition on classroom walls for (A) ventilation far from the instructor and (B) ventilation near the instructor. For each case, the left subfigure shows the bottom and two inner side walls, and the right subfigure shows the top and two outer side walls.

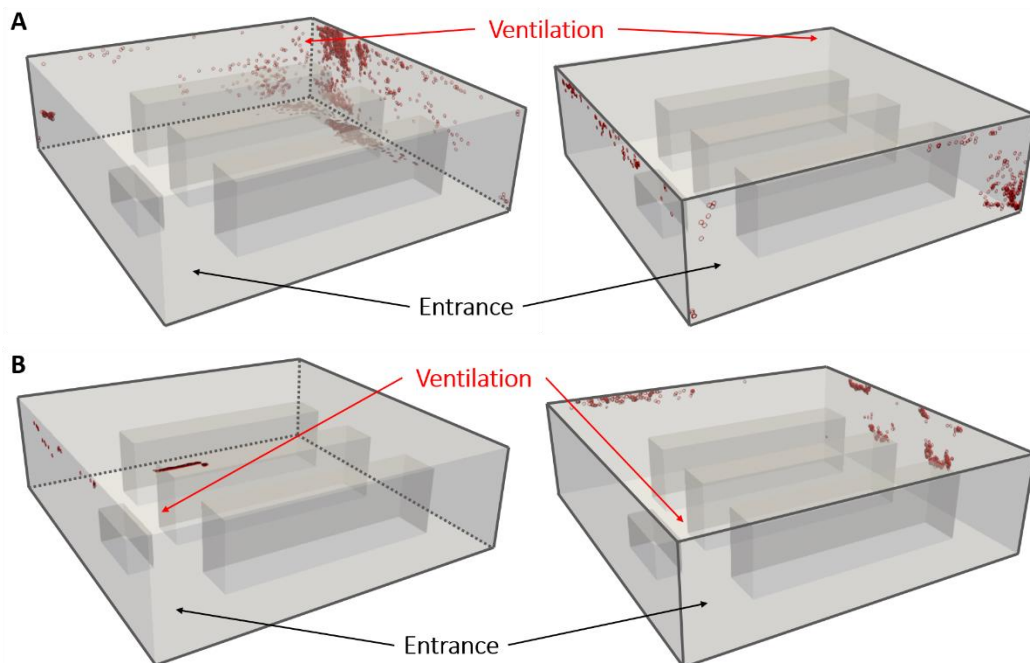


Fig. S18. Aerosol deposition on supermarket walls for (A) ventilation far from the entrance and (B) ventilation near the entrance. For each case, the left subfigure shows the bottom and two inner side walls, and the right subfigure shows the top and two outer side walls.

Participant identification	Schlieren results	
	Exhaled gas flow rate (L/s)	Breathing cone angle (°)
P1	0.07	20.3
P2	0.15	27.4
P3	0.12	30.3
P4	0.12	25.1
P5	0.08	22.7
P6	0.10	20.0
P7	0.11	27.0
P8	0.12	27.7
Average	0.11	25.0
Standard deviation	0.02	3.8

Table S1. Summary of the results from high-speed Schlieren measurements of breathing patterns.

Scenario		In the air	On the walls	Vented out
Elevator	breathing + high ventilation	78%	9%	13%
	speaking + high ventilation	80%	4%	16%
	speaking + low ventilation	99.5%	0.5%	0%
Classroom	ventilation far from the instructor	6%	88%	6%
	ventilation near the instructor	2%	88%	10%
Supermarket	ventilation far from the entrance	23%	31%	46%
	ventilation near the entrance	36%	12%	52%

Table S2. Distribution of aerosols (suspended in the air, deposited on the wall, and vented out by the ventilation system) in terms of percentage for each scenario.

References and Notes:

1. R. Anderson, H. Heesterbeek, D. Klinkenberg, T. Hollingsworth, How will country-based mitigation measures influence the course of the COVID-19 epidemic? *Lancet* **395**, 931–934 (2020).
2. J. Gralton, E. Tovey, M. McLaws, W. Rawlinson, The role of particle size in aerosolised pathogen transmission: a review. *J. Infection*, **62**(1), 1-13 (2011).
3. World Health Organization, *Practical guidelines for infection control in health care facilities*. (2004).
4. S. Asadi, N. Bouvier, A. Wexler, W. Ristenpart, The coronavirus pandemic and aerosols: Does COVID-19 transmit via expiratory particles? *Aerosol Sci. Technol.* **54**, 1–4 (2020).
5. D. Lewis, Is the coronavirus airborne? Experts can't agree. doi:10.1038/d41586-020-00974-w. *Nature* (2020)
6. K. Prather, C. Wang, R. Schooley., Reducing transmission of SARS-CoV-2. *Science*. DOI: 10.1126/science.abc6197 (2020).
7. Y. Liu, Z. Ning, Y. Chen, M. Guo, Y. Liu, N. Kumar Gali, L. Sun, Y. Duan, J. Cai, D. Westerdahl, X. Liu, K. Xu, K-F. Ho, Q. Fu, K. Lan, Aerodynamic analysis of SARS-CoV-2 in two Wuhan hospitals. *Nature*. doi:10.1038/s41586-020-2271-3 (2020).
8. N. van Doremalen, D. H. Morris, M. G. Holbrook, A. Gamble, B. N. Williamson, A. Tamin, J. L. Harcourt, N. J. Thornburg, S. I. Gerber, J. O. Lloyd-Smith, E. de Wit, V. J. Munster, Aerosol and Surface Stability of SARS-CoV-2 as Compared with SARS-CoV-1. *N. Engl. J. Med.* **382**, 1564–1567 (2020).
9. L. Zou, F. Ruan, M. Huang, L. Liang, H. Huang, Z. Hong, J. Yu, M. Kang, Y. Song, J. Xia, Q. Guo, T. Song, J. He, H. L. Yen, M. Peiris, J. Wu, SARS-CoV-2 viral load in upper respiratory specimens of infected patients. *N. Engl. J. Med.* **382**(12), 1177-1179 (2020).
10. D. A. Edwards, J. C. Man, P. Brand, J. P. Katstra, K. Sommerer, H. A. Stone, E. Nardell, G. Scheuch, Inhaling to mitigate exhaled bioaerosols. *PNAS*. **101**(50), 17383-17388 (2004).
11. P. Fabian, J. J. McDevitt, W. H. Dehaan, R. Fung, B. J. Cowling, K. H. Chan, G. M. Leung, D. K. Milton, Influenza virus in human exhaled breath: an observational study. *PloS one*. **3**(7) (2008).

12. G. R. Johnson, Morawska, L., The mechanism of breath aerosol formation. *J. Aerosol Med. Pulm. Drug Deliv.* **22**(3), 229-237 (2009).
13. R. S. Papineni, F. S. Rosenthal, The size distribution of droplets in the exhaled breath of healthy human subjects. *J. Aerosol Med.*, **10**(2), 105-116 (1997).
14. Y. H. Chao, M. P. Wan, L. Morawsaka, G. R. Johnson, Z. D. Ristovski, M. Hargreaves, K. Mengersen, S. Corbett, Y. Li, X. Xie, D. Katoshevski, Characterization of expiration air jets and droplet size distributions immediately at the mouth opening. *J. Aerosol Sci.* **40**, 122–133 (2009).
15. K. Haslbeck, K. Schwarz, J. M. Hohlfeld, J. R. Seume, W. Koch, Submicron droplet formation in the human lung. *J. Aerosol Sci.* **41**(5), 429-438 (2010).
16. G. R. Johnson, L. Morawsaka, Z. D. Ristovski, M. Hargreaves, K. Mengersen, Y. H. Chao, M. P. Wan, Y. Li, X. Xie, D. Katoshevski, S. Corbett, Modality of human expired aerosol size distributions *J. Aerosol Sci.* **42**, 839-851 (2011).
17. K. J. Heo, C. E. Lim, H. B. Kim, B. U. Lee, Effects of human activities on concentrations of culturable bioaerosols in indoor air environments. *J. Aerosol Sci.* **104**, 58-65 (2017).
18. B. Bake, P. Larsson, G. Ljungkvist, E. Ljungström, A-C Olin, Exhaled particles and small airways. *Respir. Res.* **20**(1), 8 (2019).
19. J. K. Gupta, C. H. Lin, C. H., Q. Chen, Flow dynamics and characterization of a cough. *Indoor Air*, **19**(6), 517-525 (2009).
20. L. Bourouiba, E. Dehandschoewercker, J.W. Bush, Violent expiratory events: on coughing and sneezing. *J. Fluid Mech.* **745**, 537-563 (2014).
21. G. Miserocchi, J. Milic-Emili, Effect of mechanical factors on the relation between rate and depth of breathing in cats. *J. Appl. Physiol.* **41**(3), 277-284 (1976).
22. W. F. Ganong, (1995). *Review of medical physiology*. McGraw-hill.
23. Benchetrit, G. Breathing pattern in humans: diversity and individuality. *Respir. Physiol.* **122**(2-3), 123-129 (2000).
24. V.N. Morozov, A. Y. Mikheev, A collection system for dry solid residues from exhaled breath for analysis via atomic force microscopy. *J. Breath Res.* **11**(1), 016006 (2006).
25. C. M. Powers, A new roundness scale for sedimentary particles. *J. Sediment Res.* **23**(2), 117-119 (1953).
26. R. Hamilton, G. Adie, Size, shape and elemental associations in an urban aerosol. *Sci. Total Environ.* **23**, 393-402 (1982).
27. P. Zieger, O. Väisänen, J. C. Corbin, D. G. Partridge, S. Bastelberger, M. Mousavi-Fard, B. Rosati, M. Gysel, U. K. Krieger, C. Leck, A. Nenes, I. Riipinen, A. Virtanen, M. E. Salter Revisiting the hygroscopicity of inorganic sea salt particles. *Nat. Commun.* **8**(1), 1-10 (2017).
28. J. W. Tang, The effect of environmental parameters on the survival of airborne infectious 9 agents. *J. R. Soc. Interface.* **6**, S737--S746 (2009).
29. C. Alonso, P.C. Raynor, P. R. Davies, M. Torremorell, Concentration, size distribution, and infectivity of airborne particles carrying swine viruses. *PloS one.* **10**(8) (2015).

30. Y. Zhai, X. Li, T. Wang, B. Wang, C. Li, G. Zeng, A review on airborne microorganisms in particulate matters: composition, characteristics and influence factors. *Environ. Int.* **113**, 74-90 (2018).
31. S. Asadi, A. S. Wexler, C. D. Cappa, S. Barreda, N. M. Bouvier, W. D. Ristenpart, Aerosol emission and superemission during human speech increase with voice loudness. *Sci. Rep.* **9**(1), 1-10 (2019).
32. L. Hamner, High SARS-CoV-2 attack rate following exposure at a choir practice—Skagit County, Washington, March 2020. *MMWR.* **69** (2020).
33. A. Endo, S. Abbott, A. J. Kucharski, S. Funk, Estimating the overdispersion in COVID-19 transmission using outbreak sizes outside China. *Wellcome Open Res.* **5**(67), 67 (2020).
34. Y. Liu, Z. Ning, Y. Chen, M. Guo, Y. Liu, N. K. Gali, L. Sun, Y. Duan, J. Cai, D. Westerdahl, X. Liu, Aerodynamic analysis of SARS-CoV-2 in two Wuhan hospitals. *Nature.* 1-4 (2020).
35. S. W. X. Ong, Y. K. Tan, P. Y. Chia, Y. H. Lee, O. T. Ng, M. S. Y. Wong, K. Marimuthu, Air, surface environmental, and personal protective equipment contamination by severe acute respiratory syndrome coronavirus 2 (SARS-CoV-2) from a symptomatic patient. *JAMA.* **323**(16), 1610-1612.
36. M.J. Tobin, T. Chadha, G. Jenouri, S. J. Birch, H. B. Gazeroglu, M. A. Sackner, Breathing Patterns: Normal Subjects. *Chest.* **84**, 202–205 (1983).
37. G. S. Settles, A. D. Brandt, J. D. Miller Full-scale schlieren imaging of shock waves for aviation security research. In *Proc. 8th Intl. Symp. on Flow Visualization*, ed. G. Carlomagno, Sorrento, Italy. (1998).
38. C. Xu, P. V. Nielsen, L. Liu, R. L. Jensen, G. Gong, Human exhalation characterization with the aid of schlieren imaging technique. *Build Environ.* **112**, 190-199 (2017).
39. J. W. Tang, T. J. Liebner, B. A. Craven, G. S. Settles, A schlieren optical study of the human cough with and without wearing masks for aerosol infection control. *J. R. Soc. Interface* **6**, S727-S736 (2009).
40. T. Liu, Open optical Flow. (available at <https://wmich.edu/mechanical-aerospace/opticalflow>).
41. T.-C. Poon, J.-P. Liu, Introduction to modern Digital holography with MATLAB. (Cambridge University, 2014).
42. J. Katz, J. Sheng, Applications of holography in fluid mechanics and particle dynamics. *Annu. Rev. Fluid Mech.* **42**, 531–555 (2010).
43. X. Yu, J. Hong, C. Liu, M. K. Kim, Review of digital holographic microscopy for three-dimensional profiling and tracking. *Opt. Eng.* **53**, 112306 (2014).
44. J. Lu, J. Gu, K. Li, C. Xu, W. Su, Z. Lai, D. Zhou, C. Yu, B. Xu, Z. Yang, COVID-19 outbreak associated with air conditioning in restaurant, Guangzhou, China, 2020, *Emerg. Infect. Dis.* **26**, 7 (2020).
45. W. Ranz, W. R. Marshall, Evaporation from drops. *Chem. Eng. Prog.* **48**, 141-146 (1952).
46. H. Jasak, A. Jemcov, Z. Tukovic, in *International workshop on coupled methods in numerical dynamics*. (IUC Dubrovnik Croatia, 2007), **1000**, 1-20.

47. Elevator air conditional with electric heater. (available at <https://www.qualityelev.com/main/air/aircond.htm>).
48. National Academy of Science (1977). *Accessibility: an approach to the development of design criteria and applicable design solutions*.
49. How Much Ventilation Do I Need? (available at <https://www.hvi.org/resources/publications/home-ventilation-guide-articles/how-much-ventilation-do-i-need/>)
50. V. Stadnytskyi, C. E. Bax, A. Bax, P. Anfinrud, The airborne lifetime of small speech droplets and their potential importance in SARS-CoV-2 transmission. *PNAS* **117**, 11875-11877 (2020).

Acknowledgments: We thank Hongyuan Zhang for helping out with some visualizations of the numerical data.

Funding: University of Minnesota Rapid Response Grant from Office for Vice President of Research (OVPR); University of Minnesota Institute for Engineering in Medicine (IEM) COVID-19 Rapid Response Grant program, Co-Sponsored by and the Minnesota Robotics Institute (MnRI) and the Clinical and Translational Science Institute (CTSI) through the National Center for Advancing Translational Sciences (NCATS) of the National Institutes of Health (NIH) Award Number UL1TR002494. The content is solely the responsibility of the authors and does not necessarily represent the official views of the National Institutes of Health (NIH).

Author contributions: Jiarong Hong devised the entire study. Jiarong Hong, Siyao Shao, Kevin Mallery, and Santosh Kumar designed the experiments. Siyao Shao, Jiaqi Li conducted the experiments. Siyao Shao, Ruichen He, and Jiarong Hong conducted the analysis of all the experimental data. Suo Yang and Jiarong Hong designed the numerical simulations. Dezhi Zhou and Shufan Zou conducted the numerical simulation. Suo Yang, Dezhi Zhou, Shufan Zou and Jiarong Hong conducted the analysis of numerical simulation data. Jiarong Hong, Siyao Shao, and Suo Yang wrote the paper.

Competing interests: Authors declare no competing interests.

Data and materials availability: All data is available in the main text or the supplementary materials. All data, code, and materials are hosted at the Data Repository for the University of Minnesota.